

Gravitational Collapse and Neutrino Emission of Population III Massive Stars

Ken'ichiro Nakazato¹, Kohsuke Sumiyoshi^{2,3} and Shoichi Yamada^{1,4}

nakazato@heap.phys.waseda.ac.jp

ABSTRACT

Population III (Pop III) stars are the first stars in the universe. They do not contain metals and their formation and evolution may be different from that of stars of later generations. In fact, according to the theory of star formation, Pop III stars might have very massive components ($\sim 100 - 10000M_{\odot}$). In this paper, we compute the spherically symmetric gravitational collapse of these Pop III massive stars. We solve the general relativistic hydrodynamics and neutrino transfer equations simultaneously, treating neutrino reactions in detail. Unlike supermassive stars ($\gtrsim 10^5M_{\odot}$), the stars of concern in this paper become opaque to neutrinos. The collapse is simulated until after an apparent horizon is formed. We confirm that the neutrino transfer plays a crucial role in the dynamics of gravitational collapse, and find also that the β -equilibration leads to a somewhat unfamiliar evolution of electron fraction. Contrary to the naive expectation, the neutrino spectrum does not become harder for more massive stars. This is mainly because the neutrino cooling is more efficient and the outer core is more massive as the stellar mass increases. Here the outer core is the outer part of the iron core falling supersonically. We also evaluate the flux of relic neutrino from Pop III massive stars. As expected, the detection of these neutrinos is difficult for the currently operating detectors. However, if ever observed, the spectrum will enable us to obtain the information on the formation history of Pop III stars.

¹Department of Physics, Waseda University, 3-4-1 Okubo, Shinjuku, Tokyo 169-8555, Japan

²Numazu Collage of Technology, Ooka 3600, Numazu, Shizuoka 410-8501, Japan

³Division of Theoretical Astronomy, National Astronomical Observatory of Japan, 2-21-1 Osawa, Mitaka, Tokyo 181-8588, Japan

⁴Advanced Research Institute for Science & Engineering, Waseda University, 3-4-1 Okubo, Shinjuku, Tokyo 169-8555, Japan

We investigate 18 models covering the mass range of $300 - 10^4 M_\odot$, making this study the most detailed numerical exploration of spherical gravitational collapse of Pop III massive stars. This will also serve as an important foundation for multi-dimensional investigations.

Subject headings: black hole physics — stellar dynamics — neutrinos — methods: numerical — relativity — early universe

1. Introduction

Population III (Pop III) stars are the first stars formed in the universe. Recently, lots of observational information on them have been obtained from WMAP (e.g., Spergel et al. 2003), ground-based and airborne observations of very metal-poor stars (e.g., Frebel et al. 2005), and so on. The study of Pop III stars is indispensable for the understanding of the star formation history of the universe and the galactic chemical evolution. On the other hand, theoretical studies of the first star formation suggest that Pop III stars may have a large population of very massive objects from hundreds to thousands solar mass (e.g., Nakamura & Umemura 2001) although their initial mass function (IMF) and star formation rate are still uncertain.

The evolution and fate of Pop III massive stars have been studied for a long time (e.g., Bond, Arnett, & Carr 1984 ; Fryer, Woosley, & Heger 2001). According to these studies, Pop III massive stars lose little of their mass during the quasi-static evolutions because of zero-metallicity. If an initial stellar mass is larger than $\sim 100 M_\odot$, the temperature and density are such that electron-positron pairs are created copiously at the center of the star, after the central helium depletion. This process consumes a part of thermal energy for the electron-positron rest mass, making the star unstable against gravitational collapse. It is called the pair-instability. The stellar collapse induced by the pair-instability increases the density and temperature and ignites oxygen. If the stellar mass is less than $\sim 260 M_\odot$, the rapid nuclear burning reverses the collapse and disrupts a whole star, giving rise to the so-called pair-instability supernova. On the other hand, more massive stars can not halt the collapse by nuclear burnings and emit a large amount of neutrinos before forming a black hole. These black holes will eventually have the mass of their progenitor. It is noted that the mass range is consistent with that of intermediate mass black holes, whose existence is recently suggested by observations (e.g., Maillard et al. 2004). Their origin is unknown at present.

So far, there have been a few papers studying numerically the gravitational collapse of

Pop III massive stars and the emission of neutrino accompanying it (Fryer, Woosley, & Heger 2001 ; Iocco et al. 2005). These studies are imperfect, though, in the treatment of neutrino transport and the estimate of neutrino spectrum as well as in the judgment of the black hole formation. On the other hand, there have been some detailed study of supermassive star collapse, in which neutrino emissions are taken into account together with general relativity (Linke et al. 2001). The progenitors of their concern are probably too massive (over $10^5 M_\odot$) for Pop III stars. It should be emphasized that the stars of our interest become opaque to neutrinos before black hole formation unlike the supermassive stars and that the neutrino transport should be treated appropriately.

In this paper, we calculate 18 models for the spherical gravitational collapse of Pop III massive stars with different initial masses from $300M_\odot$ to $13500M_\odot$ and numerically estimate the relic neutrino flux from them. General relativity and neutrino physics are treated rigorously. Hence the estimate of neutrino emission is accurate even when the black hole is formed. We pay particular attention to the initial mass dependence of the results.

This paper is organized as follows. In section 2, we describe the initial models and the numerical methods. In section 3, we present the numerical results with analysis. We find some evolutionary features different from what we see in the collapse of ordinary massive stars producing supernovae. We also discuss the luminosity and spectrum of emitted neutrinos and their dependence on the initial stellar mass. In section 4, we evaluate the relic neutrino flux from Pop III massive stars based on our results and the IMF recently suggested for Pop III stars. We then consider the insight into the Pop III star formation history we would obtain from a future detection of these neutrino fluxes.

2. Initial Models and Numerical Methods

2.1. Initial Models

Pop III massive stars of $\sim 100M_\odot$ to $\sim 16000M_\odot$ are supposed to start collapse by the pair-instability. In particular for stars with the mass $\gtrsim 260M_\odot$, heavy elements are burnt consecutively to form an iron core at the center. The gravitational collapse is not halted by these energy generations and a black hole is eventually formed. It is suggested (Bond, Arnett, & Carr 1984) that the iron core formed during the collapse is isentropic and the entropy per baryon is determined by the oxygen core mass. Although the fraction of helium burnt to oxygen in the helium core is uncertain, recent theoretical calculations suggest that most of helium is consumed (Umeda, & Nomoto 2002). The relation between the initial stellar mass and the helium core mass is also estimated by Bond, Arnett, & Carr (1984).

Assuming that 90% of helium becomes oxygen, we obtain the correspondence of the initial mass to the entropy per baryon of iron core as shown in Table 1. In addition, the stars with an oxygen core whose mass is $\gtrsim 8000M_{\odot}$ become unstable due to general relativistic effects before they encounter the pair-instability (Bond, Arnett, & Carr 1984). In our analysis, the oxygen core with $8000M_{\odot}$ corresponds to the initial mass $\sim 16000M_{\odot}$, the upper limit of the pair-instability given above.

In this paper, we start simulations from the iron core formation. We prepare isentropic iron cores in unstable equilibrium as initial models. Although the iron core is contracting when formed, we neglect the motion since the infalling velocity is much smaller than the velocity at the later phase, which is comparable to the light velocity. We solve the Oppenheimer-Volkoff equation to obtain the equilibrium configurations. We set the initial central temperature to be 7.7×10^9 K, a typical value for the nuclear statistical equilibrium (NSE). As already mentioned, we assume that the iron core is isentropic and the entropy per baryon is given in Table 1 (Bond, Arnett, & Carr 1984). The subsequent evolution is not so sensitive to this value. We further assume that the initial electron fraction (Y_e) equals to 0.5 in the whole core. Hence the entropy per baryon in the iron core is the only quantity which characterizes 18 models we compare in this paper (see Table 1). The equation of state is adopted from Shen et al. (1998). The original table of this equation of state is extended to $T > 100$ MeV, since we find this high temperature in some models. The method of extension is fully consistent with the original paper (Shen et al. 1998). It is noted that the equilibrium configurations obtained in this way are unstable to collapse due to the photodisintegration of iron and as a result, the core starts to collapse spontaneously without any artificial reduction of pressure in the initial models.

2.2. Numerical Methods

We compute the dynamics of spherical gravitational collapse and the neutrino transport by the general relativistic implicit Lagrangian hydrodynamics code, which solves simultaneously the neutrino Boltzmann equations (Yamada 1997 ; Yamada, Janka, & Suzuki 1999 ; Sumiyoshi et al. 2005). This code adopts the metric by Misner & Sharp (1964),

$$ds^2 = e^{2\phi(t,m)} c^2 dt^2 - e^{2\lambda(t,m)} \left(\frac{G}{c^2} \right)^2 dm^2 - r^2(t,m) (d\theta^2 + \sin^2 \theta d\phi^2), \quad (1)$$

and solves the evolution of the space-time, where c and G are the velocity of light and the gravitational constant, respectively, which are taken to be unity in the following equations, and t , m and r are the time coordinate, the baryon mass coordinate and the circumference radius, respectively. This time-slicing allows us to follow the dynamics with no difficulty

until a black hole formation. However, the original code is meant to be employed for the supernova simulation, in which gravity is not so strong. As the black hole formation is approached and gravity becomes strong, we find it better to use the following form for the matter contribution to the energy equation,

$$e^{-\phi} \left(\frac{\partial \varepsilon}{\partial t} \right)_m = -\frac{p}{\Gamma} \frac{\partial}{\partial m} (4\pi r^2 U), \quad (2)$$

where ε and p are the specific internal energy and matter pressure, and U and Γ are the radial fluid velocity and general relativistic Lorentz factor defined as

$$U = e^{-\phi} \frac{\partial r}{\partial t}, \quad (3)$$

$$\Gamma = e^{-\lambda} \frac{\partial r}{\partial m}, \quad (4)$$

respectively. This form of energy equation is used only when $\Gamma < 0.9$. We use 127 radial mesh points and set a fixed boundary condition at the outermost grid point. The radius of the outer boundary is chosen to be large enough not to affect the results.

We compute the neutrino distribution functions for 4 species of neutrino ($\nu_e, \bar{\nu}_e, \nu_\mu, \bar{\nu}_\mu$) on a discretized energy- and angular-grid points by solving the neutrino Boltzmann equations. In our simulations, the energy space is discretized to 12 mesh points and the angular space is discretized to 4 mesh points. Using a 1.5 times finer energy mesh, we find a few percent change in the total neutrino energy etc., and the qualitative feature discussed below is unchanged. As already mentioned, we consider 4 species of neutrino, $\nu_e, \bar{\nu}_e, \nu_\mu$ and $\bar{\nu}_\mu$, assuming that ν_τ and $\bar{\nu}_\tau$ are the same as ν_μ and $\bar{\nu}_\mu$, respectively. We take into account the following neutrino reactions:

[1] electron-type neutrino absorption on neutrons and its inverse,



[2] electron-type anti-neutrino absorption on protons and its inverse,



[3] neutrino scattering on nucleons,



[4] neutrino scattering on electrons,



[5] electron-type neutrino absorption on nuclei,

$$\nu_e + A \longleftrightarrow A + e^-, \quad (9)$$

[6] neutrino coherent scattering on nuclei,

$$\nu + A \longleftrightarrow \nu + A, \quad (10)$$

[7] electron-positron pair annihilation and creation,

$$e^- + e^+ \longleftrightarrow \nu + \bar{\nu}, \quad (11)$$

[8] plasmon decay and creation,

$$\gamma^* \longleftrightarrow \nu + \bar{\nu}, \quad (12)$$

[9] neutrino bremsstrahlung,

$$N + N' \longleftrightarrow N + N' + \nu + \bar{\nu}. \quad (13)$$

See Sumiyoshi et al. (2005) for the details.

3. Gravitational Collapse of Pop III Massive Stars

In this section, we summarize the numerical results of the gravitational collapse. At first we present the result of the reference model with the initial mass $M_i = 375M_\odot$, whose density and temperature profiles are shown in Fig. 1, and then we make comparison with different models. In the following, we measure the time from the point at which the apparent horizon is formed.

Just like the ordinary collapse-driven supernovae, the collapsing core is divided into two parts, to which we refer as the inner and outer cores. The inner core contracts subsonically and homologously ($U \propto r$) while the outer core infalls supersonically like free-fall $U \propto r^{-1/2}$, except for the very late phase, in which the black hole formation is imminent. We can see this structure in Fig. 2, in which we plot the radial velocity profiles at different times for the reference model. In Fig. 3, we plot also the sound speed profiles at $t = -1.52$ ms and $t = 0$ ms (the time of the apparent horizon formation) for the same model. Around $t = 0$ ms, the homology does not hold any more due to general relativistic strong gravity and the inner core splits into two parts. It is noted that the inner core is the main neutrino source especially in the late phase of collapse. This will be discussed later again.

The collapse described in this paper results in a direct black hole formation, not experiencing a bounce because of the general relativistic strong gravity. To judge the black hole

formation, we utilize apparent horizon. The apparent horizon is the outermost trapped surface. The trapped surface is the surface where both the ingoing and outgoing null geodesics have a negative expansion. The set of the trapped surfaces is called a trapped region. In the Misner-Sharp metric, the condition for the trapped region is expressed as

$$U + \Gamma < 0, \quad (14)$$

which is equivalent to

$$r < r_g \equiv 2\tilde{m}, \quad (15)$$

where \tilde{m} denotes the gravitational mass and it is related to U , Γ and r as

$$\Gamma^2 = 1 + U^2 - \frac{2\tilde{m}}{r}. \quad (16)$$

Since it is proved that the apparent horizon is always located inside the event horizon (e.g., Wald 1984), the existence of apparent horizon is a sufficient condition for the black hole formation. The apparent horizon forms off center at first, and then it is extended both inwards and outwards.

In order to emphasize the importance of neutrinos for the dynamics, we compare the results with and without neutrino transport in Fig. 4. Since the neutrino cooling is more efficient as the density increases, the neutrino emission accelerates the collapse in the central region in the early phase. As a result, the inner core becomes smaller when the neutrino is taken into account. The formation of the apparent horizon is also affected. The baryon mass coordinate where the apparent horizon forms for the first time is $4.08M_\odot$ for the model with neutrino transport, whereas that of the model without neutrino transport is $13.2M_\odot$. Moreover, the time until the apparent horizon appears becomes shorter. In Fig. 5, we show the evolution of the entropy per baryon. For the model without neutrino transport, the dynamics is adiabatic and the entropy is constant except at the shock formed around the core surface ($\sim 60M_\odot$), where the entropy is generated. For the model with neutrino transport, on the other hand, the entropy per baryon decreases because of the neutrino cooling.

We now turn to the evolutions of electron fraction (Y_e). As the electron capture proceeds, Y_e is depleted as shown in Fig. 6. Near the center, however, Y_e then starts to increase, which is not seen in the ordinary supernova core. The main reason is that the electrons are not degenerate due to high entropy in the present model and the reaction rates of electron capture and positron capture are different (e.g., Bruenn 1985). When the neutrino energy is lower than or comparable to the mass difference of proton and neutron, the electron capture dominates over the positron capture considerably. As the neutrino energy becomes higher than the mass difference and electrons are not degenerate, these two reaction rates

become comparable. As a result, the electron capture is dominant and equilibrated first, and the positron capture catches up afterward, leading to the rise of Y_e before the complete β -equilibrium. In Fig. 6, we also show the evolution of lepton fraction, Y_l . Before neutrino trapping, the Y_l profile evolves in the same way as the Y_e profile. Then, Y_l becomes unchanged and only Y_e varies after neutrino trapping. We can confirm these behaviors in the neutrino luminosities given in Fig. 7.

A large amount of neutrinos are emitted by the gravitational collapse of Pop III massive stars. The luminosity becomes as high as $\sim 10^{54}$ erg/s, much greater than the value for the ordinary supernova $\sim 10^{53}$ erg/s. However, the total energy is $\sim 10^{53}$ erg, which is comparable to the ordinary supernova. This is because the apparent horizon is formed during the collapsing phase and, as a result, the neutrino emission lasts only for ~ 100 ms.

For the stars of current interest, the neutrino sphere is formed in general before the black hole formation. It is also noted that the apparent horizon is formed inside the neutrino sphere. The neutrino optical depth $d(r)$ at the radius r is defined as

$$d(r) = \int_r^{R_s} \frac{dr'}{l_{\text{mfp}}(r')}, \quad (17)$$

where R_s is the stellar radius and l_{mfp} is the mean free path of neutrino. The radius of neutrino sphere R_ν is defined as

$$d(R_\nu) = \frac{2}{3}. \quad (18)$$

Because the mean free path depends on the energy and species of neutrino, so does the neutrino sphere.

In Fig. 8, we show the neutrino luminosity profiles and the location of the neutrino sphere for ν_e and $\bar{\nu}_e$ with several energies at $t = -12.3$ ms. At this moment, the inner core surface is located at $r = 5 \times 10^7$ cm and we can recognize that the neutrino luminosity decreases towards the center inside the inner core. This is because the interactions of neutrinos with matter are frequent enough to make the neutrino angular distribution isotropic. In the outer core, neutrinos created inside the inner core are flowing out and the neutrino angular distribution is not isotropic. In our model, the outer core is as thick as $\sim 10^9$ cm and, as a result, the neutrino sphere is far away from the inner core surface for high energy neutrinos. For instance, the optical depth of ν_e with 15.8 MeV on the inner core surface is about 4. These neutrinos are mainly emitted from the inner core and are absorbed or scattered by nucleons and electrons. As a result, the luminosity decreases mildly as neutrinos propagate from the inner core surface to the neutrino sphere. For the neutrinos with much higher energy, on the other hand, the reduction of the luminosity is steeper because the neutrino optical depth is larger, whereas the neutrino sphere for neutrinos with lower energy is close

to or inside the inner core surface.

The luminosities of low energy neutrinos increase outside the neutrino spheres. Although these low energy neutrinos have ceased to react with matter, but the neutrinos with higher energy are still scattered down to lower energy, raising the luminosities of low energy neutrinos. This is also the reason why the mean energy of neutrinos is reduced substantially from the value at the inner core surface (main neutrino source) as they propagate to the surface. It is even lower than the mean energy for the ordinary supernova. Incidentally, in the outermost region ($\gtrsim 3 \times 10^8$ cm, in Fig. 8), the neutrino luminosities decrease slightly. This reflects the difference of the emission time, that is, as the collapse goes on, the matter become denser and hotter and the neutrino emission occurs more efficiently.

We also investigate the other neutrino species, namely μ - and τ -neutrinos, and anti-neutrinos. In Fig. 9, we show the luminosity profiles and the locations of neutrino sphere for ν_μ at $t = -12.3$ ms and $t = -1.52$ ms. It is noted that we assume that ν_τ ($\bar{\nu}_\tau$) is the same as ν_μ ($\bar{\nu}_\mu$). The luminosities of ν_μ and $\bar{\nu}_\mu$ are almost identical because they have the same reactions, the difference of coupling constants is minor and Y_e is not so small. In the following, ignoring this tiny difference, we denote these 4 species as ν_x collectively. For ν_x , the radii of the neutrino spheres are smaller than those of ν_e and $\bar{\nu}_e$, since ν_x do not react via charged current processes. Outside the neutrino sphere, the negative gradient of the luminosity is steeper for ν_x than for ν_e and $\bar{\nu}_e$, especially for high energy neutrinos. The absence of the charged current reactions makes the core more optically thin for ν_x , and the rise of the temperature of the inner core is reflected more immediately by the neutrino luminosity.

It is already noted that the average energies of emitted neutrinos are rather lower than those for the ordinary supernova. The time evolutions of neutrino spectra on the surface of our computation region for the reference model are shown in Fig. 10. The spectra after $t = 0$ ms are evaluated under the assumption that the neutrinos outside the neutrino sphere flow freely. The last time in Fig. 10, $t = 85.0$ ms, is the light crossing time from the neutrino sphere for high energy neutrinos with appreciable population (roughly the location of the filled circle in the right panel of Fig. 9) to the surface. We can see that the neutrino spectra get harder as the time passes. This is because the temperature of the inner core namely becomes hotter as the collapse goes on.

We compare our results with those of Fryer, Woosley, & Heger (2001). Their non-rotation model with an initial mass of $300M_\odot$ gives a black hole at the end. The oxygen core mass is $\sim 180M_\odot$ (see Fig. 2 in their paper). We choose the reference model for comparison, since it has the same oxygen core mass $M_O \sim 180M_\odot$, though the total mass is a little bit larger, $M_i = 375M_\odot$.

The qualitative features is similar. For example, the collapsing iron core is divided into two parts, the inner and outer cores, the electron fraction (Y_e) starts to increase near the center after it decreases at first and the black hole is formed without the bounce. However, the quantitative differences can be recognized. The most outstanding one is the size of the inner core. In our model, it is $\sim 14M_\odot$ while it is $\sim 40M_\odot$ (see Fig. 3 in their paper) in their model. Although the difference is partially ascribed to the difference of the initial models, the main reason, we think, is the treatment of the neutrino transport. In their model, the neutrinos are treated in the so-called grey approximation, where only the energy-averaged distribution is employed. As demonstrated earlier, the location of neutrino sphere is highly energy-dependent. With only an average energy taken into account, the neutrino trapping will be overestimated. On the other hand, we treat multi-energy groups in our simulations, and the inner core can be cooled by low energy neutrinos. Due to this enhanced neutrino cooling, the inner core becomes smaller in our model.

The total emitted energy also differs. Our model estimates it to be $\sim 4 \times 10^{53}$ erg, which is an order of magnitude smaller than $\sim 3 \times 10^{54}$ erg in their model (see Fig. 4 in their paper). The discrepancy seems to come from the employed criterion of black hole formation. They assumed that the black hole is formed at the time when a certain fraction of the star falls within the last stable orbit, $r = 3r_g$ (e.g., Shapiro & Teukolsky 1983), while we utilized the apparent horizon formation, which is a rigorous sufficient condition, as mentioned already. This difference leads to the substantial difference of the duration of neutrino emissions. In fact, neutrino emissions last for ~ 100 ms in our model, while their estimate is ~ 1000 ms (see Fig. 4 in their paper). Note that even our estimate will be a bit over estimation, since the event horizon is located somewhat farther out from apparent horizon.

Now we move on to the comparison of different models to see the initial mass dependence of the dynamics and neutrino emissions. The qualitative features mentioned above, such as the split of the inner core or the increase of Y_e , are common to all the models. The central density, ρ_c , at the moment when the apparent horizon formed is smaller for more massive models, which is similar the results by Linke et al. (2001). For instance, we find $\rho_c = 7.51 \times 10^{14}$ g/cm³ for the reference model ($M_i = 375M_\odot$) while $\rho_c = 1.23 \times 10^{14}$ g/cm³ for the model with $M_i = 10500M_\odot$.

As the initial mass M_i gets larger, the initial value of entropy per baryon in the iron core, s_{iron} , becomes grater. Our results show that the final value of entropy per baryon at the center of core, s_{core} , does not become larger proportionately. For massive models, in fact, s_{core} is saturated. The reason is that the neutrino cooling is more efficient for more massive stars, since electrons are non-degenerate and a large amount of electron-positron pairs exist. For instance, the ratio of the net electron number to the sum of the numbers of

electron and positron at the center initially is 27.6% for the reference model while it is 5.2% for the model with $M_i = 10500M_\odot$. The existence of a large amount of electron-positron pairs leads to a smaller difference of the electron- and positron-captures. This is reflected on the minimum value of Y_e at the center, which is 0.197 in the for reference model and 0.235 in the model with $M_i = 10500M_\odot$. Owing to the very efficient neutrino cooling, the inner core mass M_{core} and the location of the apparent horizon M_{AH} at $t = 0$ ms do not increase with the initial mass M_i , either. These results are summarized in Table 2. For very massive stars, the inner core fraction gets smaller and the general relativistic strong gravity pulls not only the vicinity of the center but also the entire inner core. This makes the substructure of the inner core indiscernible by $t = 0$ ms (for example, the model with $M_i = 10500M_\odot$; Fig. 11).

The radius of the inner core, which is $\sim 3 \times 10^7$ cm for the reference model and $\sim 5 \times 10^7$ cm for the model with $M_i = 10500M_\odot$, is also insensitive to the initial mass, M_i . However, the radius of the neutrino sphere depends on M_i . For instance, The radius of the neutrino sphere for ν_e with 15.8 MeV at $t = 0$ ms is $\sim 1.5 \times 10^8$ cm for the reference model with $M_i = 375M_\odot$ while it is $\sim 10^9$ cm for the model with $M_i = 10500M_\odot$. This is mainly because more massive stars have thicker outer cores, which are opaque to neutrinos.

As mentioned already, we compute the collapse until after the apparent horizon is formed inside the inner core. Although it is likely, we do not know if the event horizon is also inside the inner core, since the null geodesics should be integrated to infinity, which is impossible. If this is the case, the black hole formation is not reflected in the neutrino signal until the inner core is swallowed into the event horizon because the inner core is the main source of neutrinos as mentioned earlier. Unfortunately, the numerical difficulty does not allow us to compute the dynamics up to the point at which the apparent horizon swallows the inner core entirely, the sufficient condition that the event horizon is outside the inner core. From the extrapolation of the previous evolutions we expect that it will take the apparent horizon ~ 1 ms to reach the inner core for all models. The neutrino emission from the inner core is estimated to be negligible in this phase. Hence, we have to somehow estimate the neutrino emissions diffusing out of the region between the inner core surface and the neutrino sphere. We can obtain the upper and lower limits as follows. The upper limit is estimated assuming that all neutrinos in this region flow out without absorbed or scattered. For the lower limit, on the other hand, we assume that all neutrinos in this region are trapped and do not come out. We summarize the average and total energies of emitted neutrinos estimated in this way for all the models in Table 3.

In Fig. 12, we plot the time-integrated energy and number spectra of neutrinos for 4 different models based on the upper limit discussed above. As expected, the more massive

the initial mass is, the larger the total emission energy is, since the liberated gravitational energy is greater. It is interesting, however, that the spectra do not become harder but rather softer as the initial mass increases. There are two reasons. The first reason is again that the neutrino cooling is more efficient for more massive stars, and as a result that, the physical condition of the inner core, which is a main source of neutrinos, is similar among different models. The second reason, which is also mentioned already, is that massive models have a very thick outer core which prevents high energy neutrinos from getting out of the inner core directly. As seen in Table 3, this is particularly remarkable for ν_x , the species with the lowest reaction rates. The reason is as follows. The distance from the stellar surface down to the neutrino sphere is almost independent of the initial mass. On the other hand, the distance from the surface of the inner core, the main neutrino source, to the stellar surface is dependent on it. As the initial mass increases, so does the distance between the inner core surface and the neutrino sphere. Since the neutrino sphere for ν_x is inside of those for ν_e and $\bar{\nu}_e$ and the temperature scale height is smaller near the inner core, the average energy of ν_x is more sensitive to the difference of the initial mass.

4. Relic Neutrinos from Pop III Massive Stars

In this section, we estimate the number flux of diffuse relic neutrinos from Pop III massive stars. After giving the formulation, we apply it to several star formation histories, and discuss the possibility to constrain them. In the following, we do not take into account the mixing of neutrinos for simplicity.

4.1. Formulation for Relic Neutrino Background

Here we formulate the number flux of the relic neutrino from Pop III massive stars. We assume that Pop III stars in the mass interval $M_0 \leq m \leq M_N$ collapse and emit neutrinos at redshift $z_i \geq z \geq z_f$. Then the present number flux of relic neutrinos on the earth is given by

$$\frac{dF_\nu}{dE_\nu} = c \int_{z_i}^{z_f} \int_{M_0}^{M_N} \frac{dN(m, E'_\nu)}{dE'_\nu} (1+z) R_{\text{PopIII}}(z, m) dm \frac{dt}{dz} dz, \quad (19)$$

where E_ν is the detected neutrino energy and $E'_\nu = (1+z)E_\nu$ is the emitted neutrino energy. The neutrino number spectrum emitted by the progenitor with mass m is $dN(m, E'_\nu)/dE'_\nu$. We denote the birth rate of Pop III massive stars per comoving volume per mass as $R_{\text{PopIII}}(z, m)$. Massive stars are supposed to die immediately after the birth. The relation between t and

z is given by

$$\frac{dz}{dt} = -H_0(1+z)\sqrt{\Omega_m(1+z)^3 + \Omega_\Lambda}, \quad (20)$$

and according to the standard Λ CDM cosmology, the cosmological parameters are given as $\Omega_m = 0.3$, $\Omega_\Lambda = 0.7$ and $H_0 = 71_{-3}^{+4}$ km/s/Mpc (Spergel et al. 2003).

Here we assume that $R_{\text{PopIII}}(z, m)$ can be written as

$$R_{\text{PopIII}}(z, m) dm dz = \frac{dn(m)}{dm} dm \psi(z) dz = dn(m) \psi(z) dz, \quad (21)$$

where $dn(m)$ is the number of Pop III massive stars within the mass interval $[m, m + dm]$. The normalization factor $\psi(z)$ is chosen as

$$\int_{z_i}^{z_f} \psi(z) \frac{dt}{dz} dz = \int_{z_f}^{z_i} \frac{\psi(z)}{H_0(1+z)\sqrt{\Omega_m(1+z)^3 + \Omega_\Lambda}} dz = 1, \quad (22)$$

Thus we can rewrite eq. (19) as

$$\frac{dF_\nu}{dE_\nu} = c \int_{M_0}^{M_N} dm \frac{dn(m)}{dm} \int_{z_f}^{z_i} dz \frac{\psi(z)}{H_0(1+z)\sqrt{\Omega_m(1+z)^3 + \Omega_\Lambda}} \frac{dN(m, E'_\nu)}{dE'_\nu} (1+z). \quad (23)$$

In the above equation, $dn(m)/dm$ represents the initial mass function (IMF). Here we adopt the IMF of Pop III stars proposed by Nakamura & Umemura (2001). Their IMF is bimodal and the heavier component is given as

$$\begin{cases} \frac{dn}{dm} = Bm^{-\beta-1} & \text{for } m \geq M_{\min}, \\ n = 0 & \text{for } m < M_{\min}, \end{cases} \quad (24)$$

where $\beta > 1$ and $B > 0$ are independent of m . Incidentally, the IMF given by Salpeter (1955) has $\beta = 1.35$ for the mass range, $0.4M_\odot < m < 10M_\odot$. The mass density of Pop III massive stars is given as

$$P_{\text{all}} = \int_{M_{\min}}^{\infty} m dn = \frac{B}{\beta - 1} M_{\min}^{1-\beta}. \quad (25)$$

On the other hand, we denote the time-integrated fraction of cosmic baryon converted into Pop III stars as ϵ and the fraction of the mass contained in the heavier population as $(1 - \kappa)$. Then P_{all} can be also expressed as

$$P_{\text{all}} = n_b m_N \epsilon (1 - \kappa), \quad (26)$$

where $n_b = (2.5 \pm 0.1) \times 10^{-7} \text{ cm}^{-3}$ is the present number density of cosmic baryon (Spergel et al. 2003) and m_N is the nucleon mass. From eqs. (25) and (26), we can determine the normalization factor B as

$$B = (\beta - 1) M_{\min}^{\beta-1} n_b m_N \epsilon (1 - \kappa). \quad (27)$$

In order to evaluate the relic neutrino flux from our models, we approximate the integral in eq. (23) by the summation over mass bins covering the mass range of our models. Using the equation

$$\int_{M_{k-1}}^{M_k} dm \frac{dn(m)}{dm} = \frac{\beta - 1}{\beta} n_b m_N \epsilon (1 - \kappa) M_{\min}^{\beta-1} (M_{k-1}^{-\beta} - M_k^{-\beta}), \quad (28)$$

we rewrite eq. (23) as

$$\begin{aligned} \frac{dF_\nu}{dE_\nu} = & \frac{\beta - 1}{\beta} c n_b m_N \epsilon (1 - \kappa) M_{\min}^{\beta-1} \sum_{k=1}^N (M_{k-1}^{-\beta} - M_k^{-\beta}) \\ & \times \int_{z_f}^{z_i} dz \frac{\psi(z)}{H_0(1+z)\sqrt{\Omega_m(1+z)^3 + \Omega_\Lambda}} \frac{dN(\widetilde{M}_k, E'_\nu)}{dE'_\nu} (1+z), \end{aligned} \quad (29)$$

where \widetilde{M}_k is approximated by the geometric mean of M_{k-1} and M_k , and is chosen to coincide with the mass of our models. M_k is independent of β and given in Table 4. This approximation is estimated to give at most several percents of error for the range of $1 < \beta < 3$. Here we use 18 mass bins starting from $M_0 = 260M_\odot$, the largest mass for the pair-instability supernova, to $M_{18} = 16000M_\odot$, the smallest mass for the onset of collapse by the general relativistic effect.

In the following, we take the most optimistic values for the uncertain quantities in estimating the relic neutrinos. For the total neutrino emissions, we take the upper limit given in Table 3. In the IMF by Nakamura & Umemura (2001), we choose $(1 - \kappa) = 1$. Since they estimate that M_{\min} is in the range of a few times $10 - 100M_\odot$, we take $M_{\min} = 100M_\odot$. The Pop III star formation efficiency, ϵ , one of the most uncertain factors, is suggested to be rather large, of the order of 10%, from the estimations of the contribution of Pop III stars to the cosmic infrared background (e.g., Santos, Bromm, & Kamionkowski 2002 ; Salvaterra, & Ferrara 2003 ; However, see also Madau, & Silk 2005). Here we assume $\epsilon = 0.1$. The change of the relic neutrino flux due to the variations of $(1 - \kappa)$, M_{\min} or ϵ is obtained from eq. (29). We find that these parameters do not affect the peak energy of neutrino. β is also an uncertain parameter, and its influence on the flux is complicated. Hence we take several values.

As for the star formation history, $\psi(z)$, we employ the following three models. The observation by WMAP suggests that the reionization occurred at redshift $z = 17 \pm 5$ (Spergel et al. 2003). Based on this, we assume the following function for $\psi(z)$ as model A.

$$\psi(z) = \psi_A(z) \equiv \frac{1}{5\sqrt{2\pi}} \exp\left(-\frac{(z-17)^2}{20}\right) H_0 (1+z) \sqrt{\Omega_m(1+z)^3 + \Omega_\Lambda}. \quad (30)$$

On the other hand, according to the theoretical investigation of the star formation history by Scannapieco, Schneider, & Ferrara (2003), the peak of the Pop III star formation might have been at $z \sim 10$. Hence, as model B,

$$\psi(z) = \psi_B(z) \equiv \delta(z-10) H_0 (1+z) \sqrt{\Omega_m(1+z)^3 + \Omega_\Lambda}. \quad (31)$$

Some authors attempt to estimate the Pop III star formation rate using the gamma ray bursts (Yonetoku et al. 2004 ; Murakami et al. 2005), and suggest a rather continuous formation of Pop III stars. Based on their results, $\psi(z)$ is assumed to be

$$\psi(z) = \psi_C(z) \propto (1+z)^{1.7} \quad \text{for } 4 < z < 12, \quad (32)$$

in model C.

4.2. Results and Discussion

In Fig. 13, we plot the relic neutrino fluxes for model A and $\beta = 1.35$. It is seen that the peak energy of ν_x ($= \nu_\mu, \nu_\tau, \bar{\nu}_\mu, \bar{\nu}_\tau$) is smaller than ν_e and $\bar{\nu}_e$. At first glance, this seems inconsistent with the trend of the average energy shown in Table 3. However, the number flux of ν_x has a high energy tail because of the absence of charged current reactions. Integrated over the spectrum, the mean energy of ν_x becomes higher than those of ν_e and $\bar{\nu}_e$ as in Table 3.

We show in the left panel of Fig. 14 the relic $\bar{\nu}_e$ fluxes for different values of β . We find that the peak energy is not sensitive to β . This is due to the fact that the mean energy of the neutrinos is insensitive to the initial stellar mass, which we have already mentioned. We also find that the model with $\beta = 1.35$ gives the greatest number flux. This can be understood as follows. We first remind readers that the total mass density, P_{all} , is fixed when we vary β (see eqs. (25) and (26)). If β is close to unity, a substantial fraction of stars falls in the realm of supermassive stars ($\gtrsim 16000M_\odot$), which we ignore in this paper. The same is true for larger β . In this case, a large population of stars contribute to the pair-instability supernovae ($\lesssim 260M_\odot$), which are not considered here, either. In the right panel of Fig. 14, we compare different star formation histories. It is found that the larger the redshift at which Pop III

massive stars are formed is, the lower the peak energy becomes. We have seen that the peak energy is not sensitive to IMF. Hence the peak energy is determined solely by the redshift of the Pop III star formation.

As for the possibilities of detection, we must say that it is difficult for the currently operating detectors. In spite of the difference of our results and what is found by Iocco et al. (2005) based on the results by Fryer, Woosley, & Heger (2001), both results are negative for detection, because the cosmological redshift reduces the peak energy to lower values. To put it more precisely, the relic ν_e fluxes from Pop III massive stars are overwhelmed by solar ν_e below 18 MeV and relic neutrinos by ordinary supernova above ~ 10 MeV. As for $\bar{\nu}_e$, the emissions from nuclear reactors are the main obstacle below 10 MeV. Thus the existing detectors can not distinguish Pop III relic neutrinos from others. However, because the solar and reactor neutrinos are not isotropic, removing them is possible at least in principle. For $\bar{\nu}_e$, in particular, Pop III massive stars are the largest cosmological sources. In the future, we may be able to discuss the Pop III star formation history with these diffuse neutrino fluxes.

5. Conclusions

In this paper, we have numerically studied the spherical gravitational collapse of the Pop III massive stars, taking into account the reactions and transports of neutrinos in detail. Neutrinos affect the dynamics of collapse crucially, determining the inner core mass, the location and formation time of the apparent horizon. Moreover, it gives rise to the non-monotonic evolution of the electron fraction during the collapse, which is not seen in the ordinary supernova core. Neutrino cooling is very efficient and the final value of core entropy is not sensitive to the initial value or the initial stellar mass. For very massive stars, even the outer core becomes opaque to neutrinos. As a result, the neutrino spectra do not become harder as the initial mass increases. Therefore, the peak energy of relic neutrinos is mainly determined by the redshift of the Pop III star formation and not sensitive to the IMF. At present, the detection of these relic neutrinos is highly difficult.

These Pop III massive stars might have been rotating rapidly and have had magnetic fields, both of which we ignored in this paper. Although the numerical treatment of general relativity and neutrino transport in multi-dimension is a challenging problem, rapidly rotating Pop III massive stars with magnetic fields are proposed to be associated with gamma ray bursts (e.g., Schneider et al. 2002), and it is certainly worth investigation.

One of the authors (K.N.) is grateful to Hideki Maeda for valuable discussions. He would like to thank Hideyuki Suzuki for useful comments and aids in computations. In this work,

numerical computations were partially performed on Fujitsu VPP5000 at the Astronomical Data Analysis Center, ADAC, of the National Astronomical Observatory of Japan (VPP5000 System Projects rkn60c, wkn10b), and on the supercomputers in RIKEN and KEK (KEK Supercomputer Project No. 108). This work was partially supported by Grants-in-Aid for the Scientific Research from the Ministry of Education, Science and Culture of Japan through No.14079202, No.14740166, No.15740160, and The 21st century COE Program “Holistic Research and Education Center for Physics of Self-organization Systems”.

REFERENCES

- Ando, S., & Sato, K. 2004, *New J. Phys.*, 6, 170
- Bond, J.R., Arnett, W.D., & Carr, B.J. 1984, *ApJ*, 280, 825
- Bruenn, S.W. 1985, *ApJS*, 58, 771
- Frebel, A., et al. 2005, *Nature*, 434, 871
- Fryer, C.L., Woosley, S.E., & Heger, A. 2001, *ApJ*, 550, 372
- Herant, M., Benz, W., Hix, W.R., Fryer, C.L., & Colgate, C.A. 1994, *ApJ*, 435, 339
- Iocco, F., Mangano, G., Miele, G., Raffelt, G.G., & Serpico, P.D. 2005, *Astropart. Phys.*, 23, 303
- Linke, F., Font, J.A., Janka, H.-Th, Müller, E., & Papadopoulos, P. 2001, *A&A*, 376, 568
- Madau, P., & Silk, J. 2005, *MNRAS*, 359, L37
- Maillard, J.P., Paumard, T., Stolovy, S.R., & Rigaut, F. 2004, *A&A*, 423, 155
- Misner, C.W., & Sharp, D.H. 1964, *Phys. Rev.*, 136, 571
- Murakami, T., et al. 2005, *ApJ*, 625, L13
- Nakamura, F., & Umemura, M. 2001, *ApJ*, 548, 19
- Salpeter, E.E. 1955, *ApJ*, 122, 161
- Salvatterra, R., & Ferrara, A. 2003, *MNRAS*, 339, 973
- Santos, M.R., Bromm, V., & Kamionkowski, M. 2002, *MNRAS*, 336, 1082
- Scannapieco, E., Schneider, R., & Ferrara, A. 2003, *ApJ*, 589, 35

- Schneider, R., Ferrara, A., Natarajan, P., & Omukai, K. 2002, *ApJ*, 571, 30
- Shapiro, S.L., & Teukolsky, S.A. 1983, in *Black Holes, White Dwarfs, and Neutron Stars* (New York:Wiley)
- Shen, H., Toki, H., Oyamatsu, K., & Sumiyoshi, K. 1997, *Prog. Theor. Phys.*, 100, 1013
- Shen, H., Toki, H., Oyamatsu, K., & Sumiyoshi, K. 1997, *Nucl. Phys.*, A637, 435
- Suzuki, H. 1990, Ph.D. thesis, Univ. Tokyo
- Spergel, D.N., et al. 2003, *ApJS*, 148, 174
- Strigari, L.E., Kaplinghat, M., Steigman, G., & Walker, T.P. 2004, *J. Cosmol. Astropart. Phys.*, 0403, 007
- Sumiyoshi, K., Yamada, S., Suzuki, H., Shen, H., Chiba, S., & Toki, H. 2005, *ApJ*, in Press.
- Umeda, H., & Nomoto, K. 2002, *ApJ*, 565, 385
- van Riper K.A. 1979, *ApJ*, 232, 558
- Wald, R.M. 1984, in *General Relativity* (Chicago and London:The University of Chicago Press)
- Woosley, S.E., Heger, A., & Weaver, T.A. 2002, *Rev. Mod. Phys.*, 74, 1015
- Yamada, S. 1997, *ApJ*, 475, 720
- Yamada, S., Janka, H.-Th, & Suzuki, H. 1999, *A&A*, 344, 533
- Yonetoku, D., et al. 2004, *ApJ*, 609, 935

Table 1: Correspondence of the Initial Mass to the Iron Core Entropy

M_i	M_{He}	M_{O}	s_{O}	s_{iron}
300	159	143	14.54	15.98
375	201	181	16.06	17.50
470	254	228	17.73	19.17
585	319	287	19.53	20.96
730	400	360	21.54	22.97
915	504	454	23.81	25.25
1145	633	570	26.33	27.77
1430	794	714	29.10	30.54
1800	1001	901	32.29	33.74
2250	1254	1129	35.74	37.19
2800	1563	1407	39.51	40.96
3500	1956	1760	43.79	45.24
4350	2434	2191	48.44	49.89
5500	3080	2772	54.04	55.50
6800	3810	3429	59.70	61.16
8500	4765	4288	66.32	67.78
10500	5889	5300	73.29	74.75
13500	7574	6817	82.59	84.06

Note. — M_i , M_{He} and M_{O} denote the initial stellar mass, helium core mass and oxygen core mass respectively, and they are in the unit of the solar mass (M_{\odot}). The entropy per baryon in the oxygen core and the iron core is denoted as s_{O} and s_{iron} , respectively, and they are in the unit of the Boltzmann constant (k_{B}).

Table 2: Initial Mass Dependence of Core Entropy, Core Mass and Location of Apparent Horizon.

M_i	s_{iron}	s_{core}	M_{core}	M_{AH}
300	15.98	7.33	13.6	4.17
375	17.50	7.37	14.1	4.08
470	19.17	7.70	15.8	4.53
585	20.96	7.88	16.8	4.84
730	22.97	8.07	18.2	5.18
915	25.25	8.28	19.5	5.39
1145	27.77	8.50	21.0	5.82
1430	30.54	8.77	23.4	6.33
1800	33.74	8.90	24.7	6.46
2250	37.19	9.24	26.5	6.96
2800	40.96	9.64	30.0	7.60
3500	45.24	10.10	33.5	8.42
4350	49.89	10.35	36.0	8.44
5500	55.50	10.56	39.0	9.11
6800	61.16	10.41	37.6	9.10
8500	67.78	10.58	40.1	9.40
10500	74.75	10.48	39.5	9.26
13500	84.06	11.20	44.5	9.91

Note. — M_i and s_{iron} are the same as in Table 1. s_{iron} is the entropy per baryon at the center of the inner core at $t = 0$, and it is in the unit of the Boltzmann constant (k_B). M_{core} is the mass of the inner core at $t = 0$ and M_{AH} is the location of the apparent horizon at $t = 0$. They are in the unit of the solar mass (M_\odot).

Table 3. Estimates of Average and Total Energies of Emitted Neutrinos.

M_i	$\langle E_{\nu_e} \rangle$	$\langle E_{\bar{\nu}_e} \rangle$	$\langle E_{\nu_x} \rangle$	$E_{\nu_e,52}^{\text{tot}}$	$E_{\bar{\nu}_e,52}^{\text{tot}}$	$E_{\nu_x,52}^{\text{tot}}$	$E_{\text{all},52}^{\text{tot}}$
300	5.30 - 5.33	8.00 - 8.04	10.21 - 10.89	12.77 - 12.87	9.58 - 9.69	2.54 - 2.78	32.49 - 33.69
375	5.06 - 5.10	7.20 - 7.28	8.26 - 8.98	17.16 - 17.38	12.81 - 13.10	3.04 - 3.41	42.14 - 44.10
470	5.27 - 5.33	7.57 - 7.68	8.46 - 9.09	23.83 - 24.21	18.80 - 19.35	3.58 - 3.93	56.90 - 59.27
585	5.22 - 5.28	7.36 - 7.45	7.66 - 8.11	31.31 - 31.82	25.94 - 26.60	4.38 - 4.72	74.76 - 77.30
730	5.18 - 5.24	7.16 - 7.25	7.10 - 7.43	41.90 - 42.62	35.75 - 36.67	5.69 - 5.96	100.1 - 103.1
915	5.13 - 5.20	6.98 - 7.07	6.66 - 6.90	56.39 - 57.48	49.41 - 50.79	7.50 - 7.84	135.8 - 139.6
1145	5.08 - 5.16	6.79 - 6.89	6.35 - 6.53	75.57 - 77.21	67.71 - 69.67	10.29 - 10.66	184.4 - 189.5
1430	5.03 - 5.11	6.62 - 6.72	6.05 - 6.19	101.7 - 103.9	92.64 - 95.36	14.20 - 14.59	251.1 - 257.6
1800	5.01 - 5.09	6.52 - 6.62	6.03 - 6.20	135.0 - 138.5	127.6 - 131.5	20.02 - 20.82	342.7 - 353.3
2250	4.88 - 4.97	6.21 - 6.32	5.66 - 5.83	182.3 - 187.4	171.2 - 177.2	28.63 - 29.88	468.1 - 484.1
2800	4.89 - 4.99	6.16 - 6.28	5.69 - 5.90	248.3 - 256.2	236.6 - 245.3	41.60 - 43.96	651.3 - 677.3
3500	4.83 - 4.93	6.00 - 6.14	5.60 - 5.81	330.3 - 341.8	320.6 - 333.9	59.91 - 63.44	890.6 - 929.5
4350	4.73 - 4.83	5.83 - 5.95	5.44 - 5.63	422.5 - 437.5	424.7 - 441.3	82.79 - 87.36	1178 - 1228
5500	4.63 - 4.74	5.64 - 5.76	5.29 - 5.46	562.3 - 582.2	575.5 - 596.7	117.2 - 123.4	1608 - 1672
6800	4.47 - 4.55	5.36 - 5.46	5.00 - 5.11	695.2 - 715.1	728.3 - 749.7	148.6 - 163.8	2018 - 2194
8500	4.35 - 4.43	5.15 - 5.23	4.58 - 4.67	899.2 - 924.6	952.3 - 979.1	202.8 - 209.4	2663 - 2741
10500	4.05 - 4.12	4.92 - 4.99	4.31 - 4.38	1124 - 1152	1204 - 1233	261.5 - 267.5	3374 - 3455
13500	3.94 - 4.00	4.75 - 4.82	4.20 - 4.28	1558 - 1597	1669 - 1712	388.2 - 398.4	4780 - 4902

Note. — The mean energy of emitted ν_i is denoted as $\langle E_{\nu_i} \rangle \equiv E_{\nu_i}^{\text{tot}}/N_{\nu_i}^{\text{tot}}$ and the lower and upper limits of them are given in the unit of MeV, where $E_{\nu_i}^{\text{tot}}$ and $N_{\nu_i}^{\text{tot}}$ are the total energy and number of neutrinos. The subscript “52” means the quantity given in the unit of 10^{52} erg. $E_{\text{all}}^{\text{tot}}$ is the total energy summed over all species.

Table 4: Binning of IMF

k	0	1	2	3	4	5	6	7	8	9
M_k	260	335	420	525	655	815	1025	1280	1600	2010
k	10	11	12	13	14	15	16	17	18	
M_k	2500	3150	3900	4900	6100	7600	9450	11650	16000	

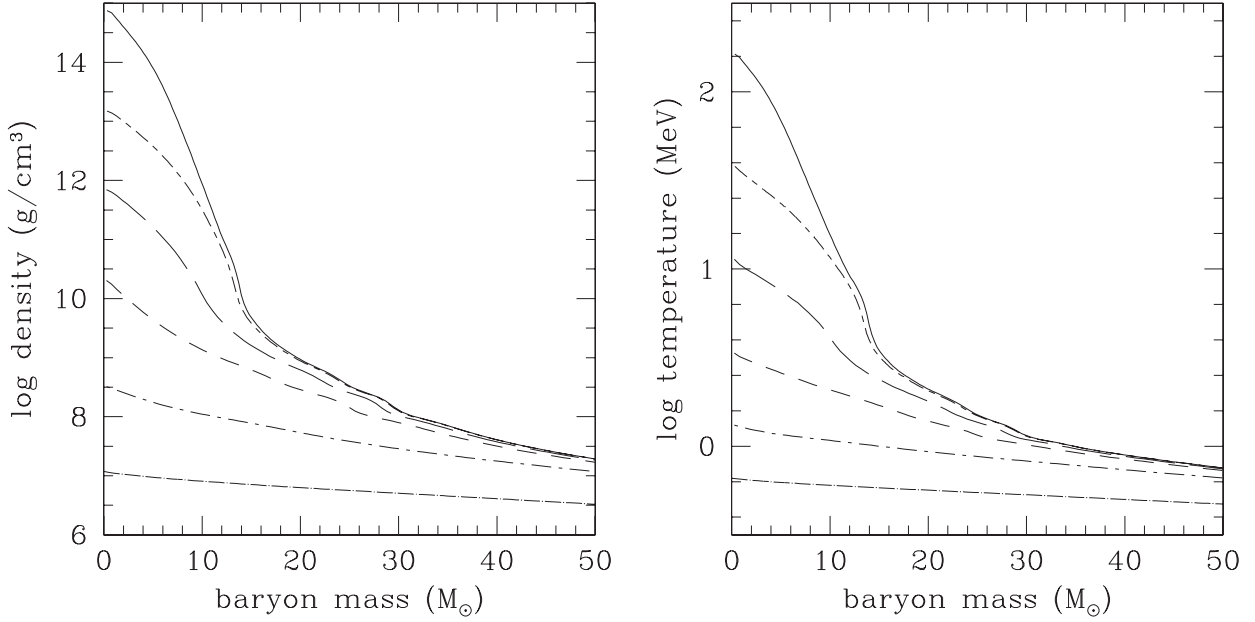


Fig. 1.— Density (left) and temperature (right) profiles for the model with $M_i = 375M_\odot$. The lines correspond, from bottom to top, to $t = -8.88$ s, $t = -239$ ms, $t = -41.6$ ms, $t = -12.3$ ms, $t = -1.52$ ms and $t = 0$ ms.

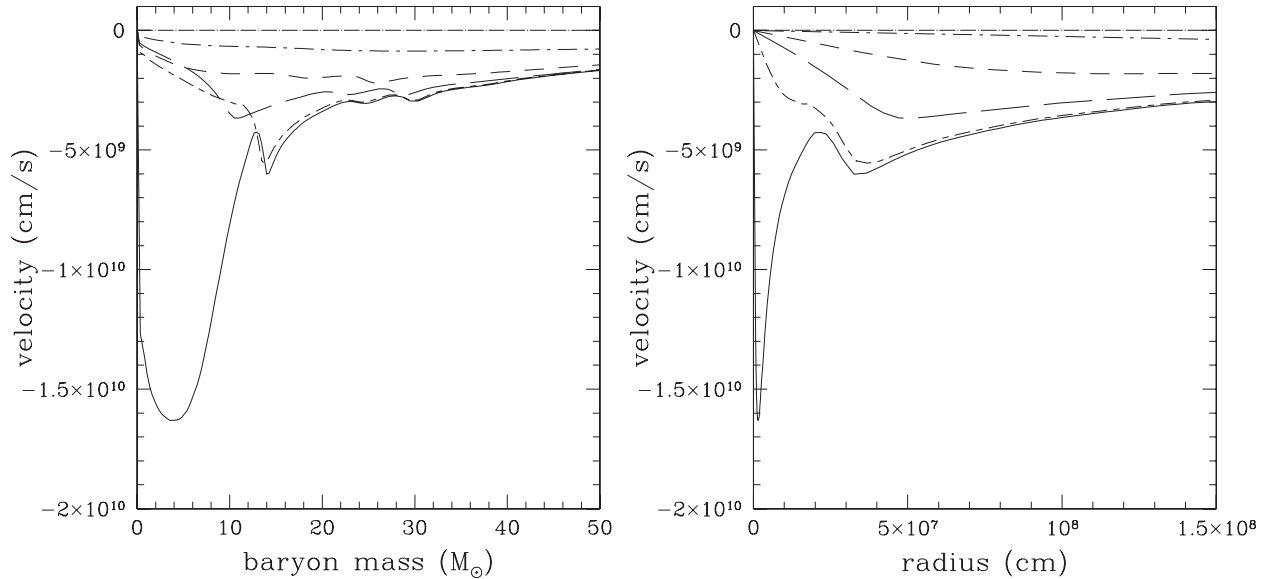


Fig. 2.— Profiles of the radial velocity for the model with $M_i = 375M_\odot$. The notation of lines is the same as in Fig. 1.

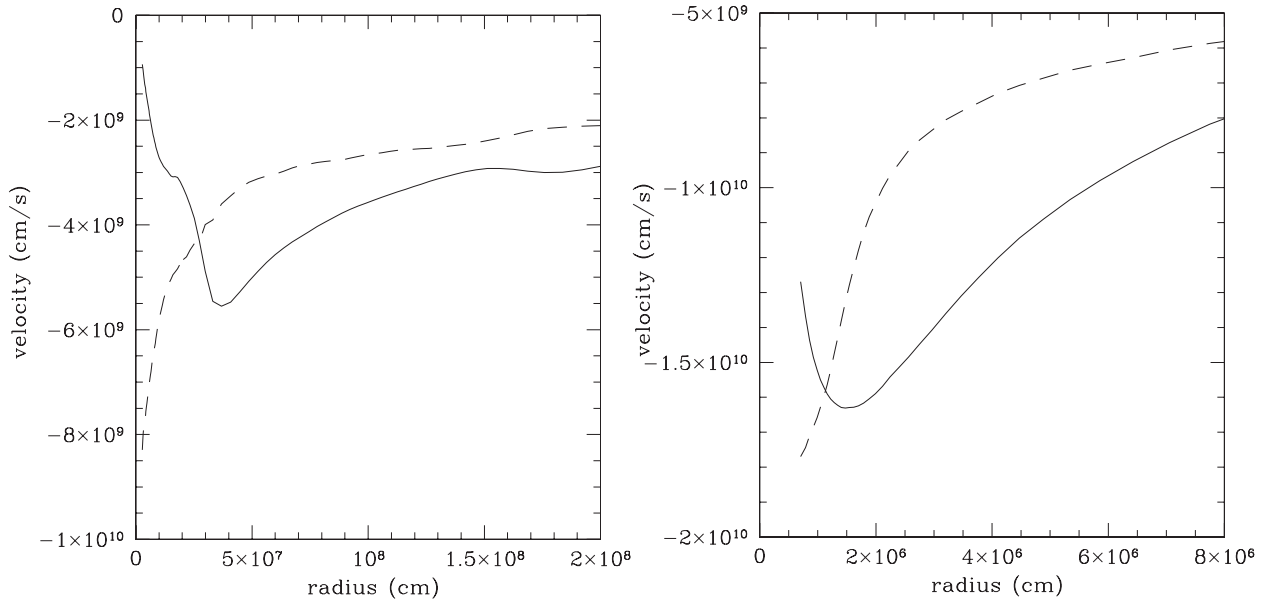


Fig. 3.— Profiles of the radial velocity (solid line) and the sound speed (dashed line). The left panel is for $t = -1.52$ ms and the right one is for $t = 0$ ms.

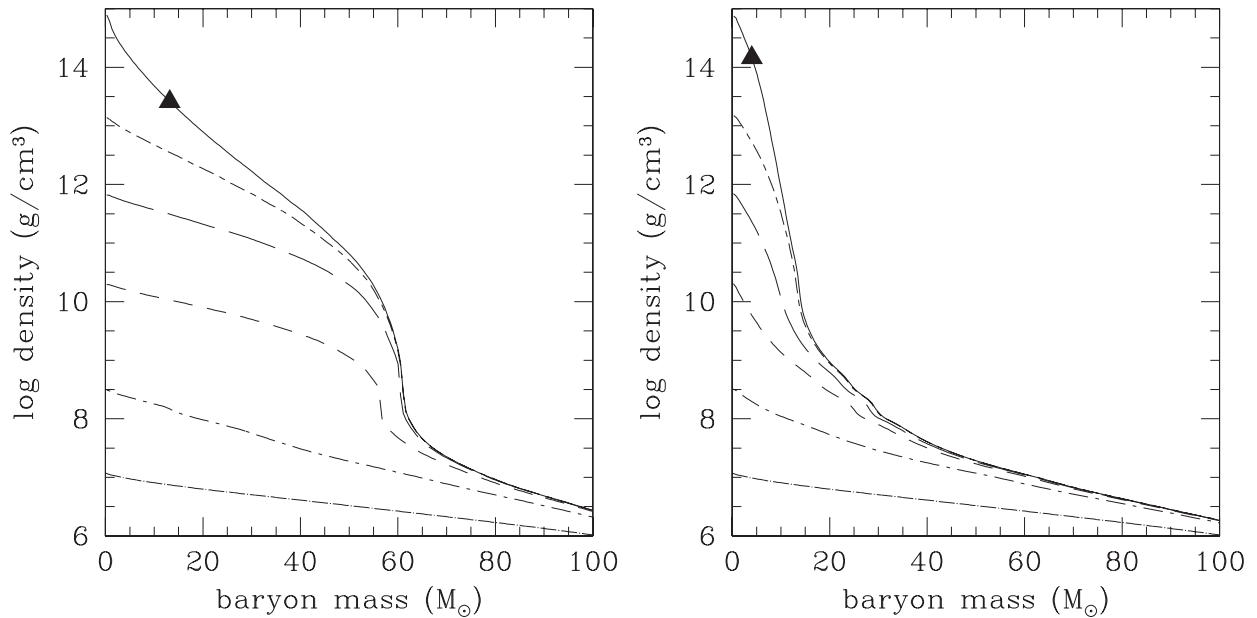


Fig. 4.— Comparison of the results without (left) and with (right) neutrinos for the same model with $M_i = 375M_\odot$. In the each panel, the triangles show the locations of the apparent horizon. In the left panel, the lines correspond, from bottom to top, to $t = -12.0$ s, $t = -343$ ms, $t = -42.3$ ms, $t = -4.92$ ms, $t = -0.699$ ms and $t = 0$ ms. The right panel is the same as the left panel in Fig. 1.

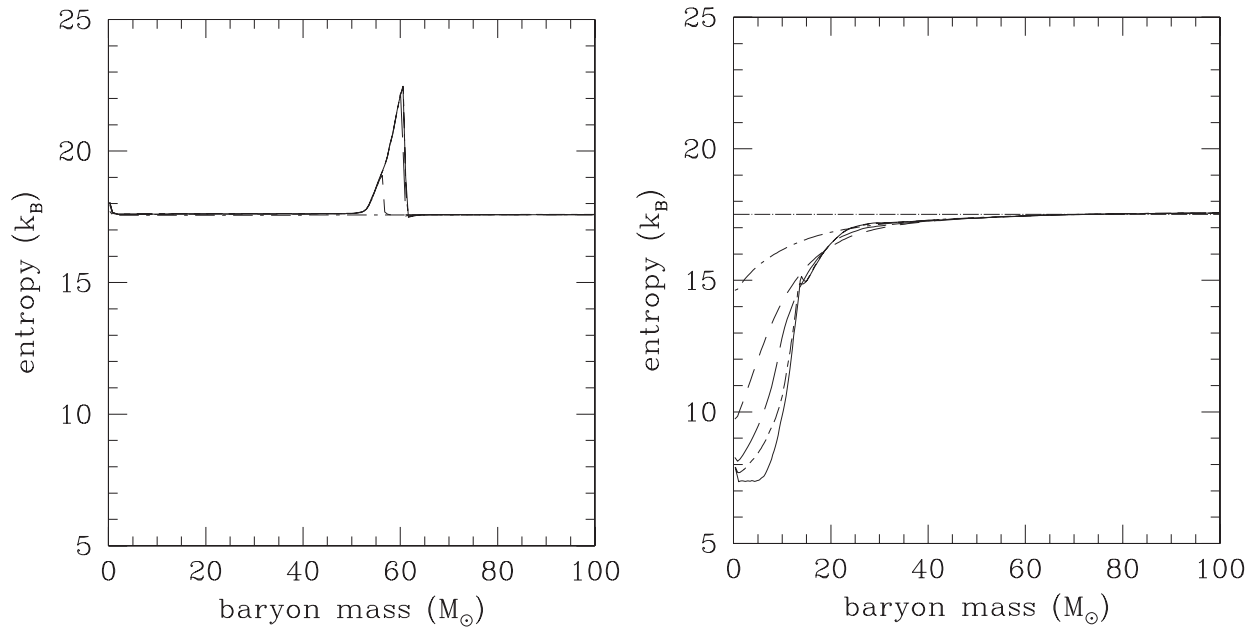


Fig. 5.— The entropy profiles for the model with $M_i = 375M_\odot$ without (left) and with (right) neutrinos. The notation is the same as in Fig. 4

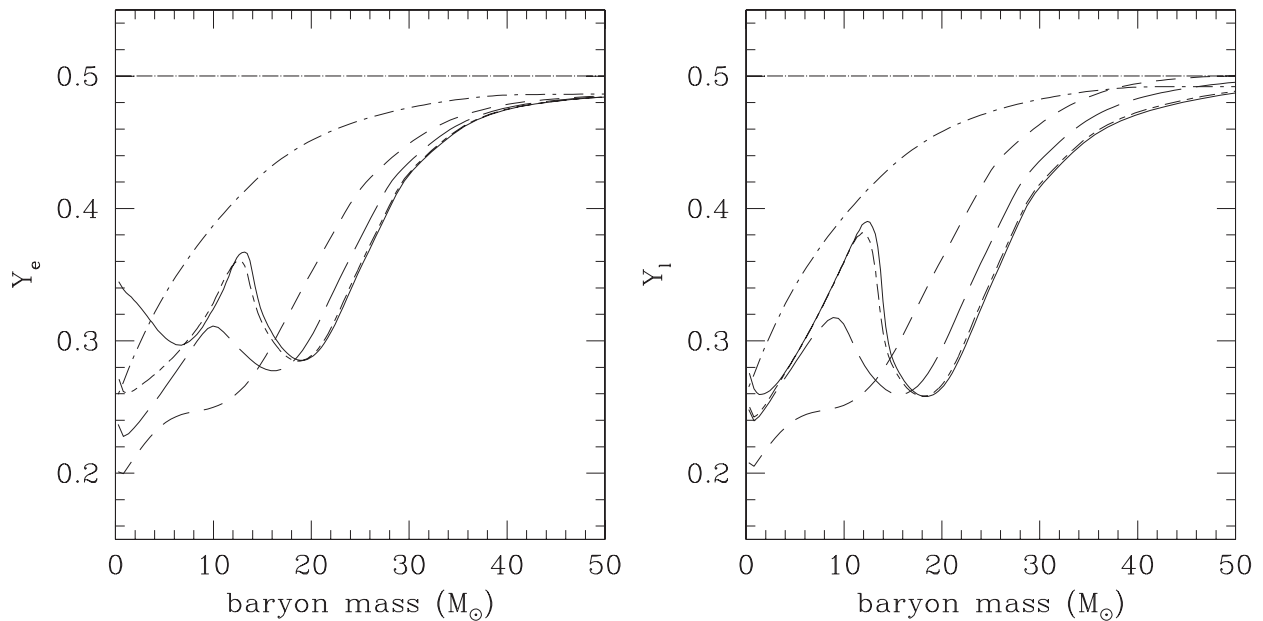


Fig. 6.— Profiles of Y_e (left) and Y_l (right) for the model with $M_i = 375M_\odot$. The notation of lines is the same as in Fig. 1.

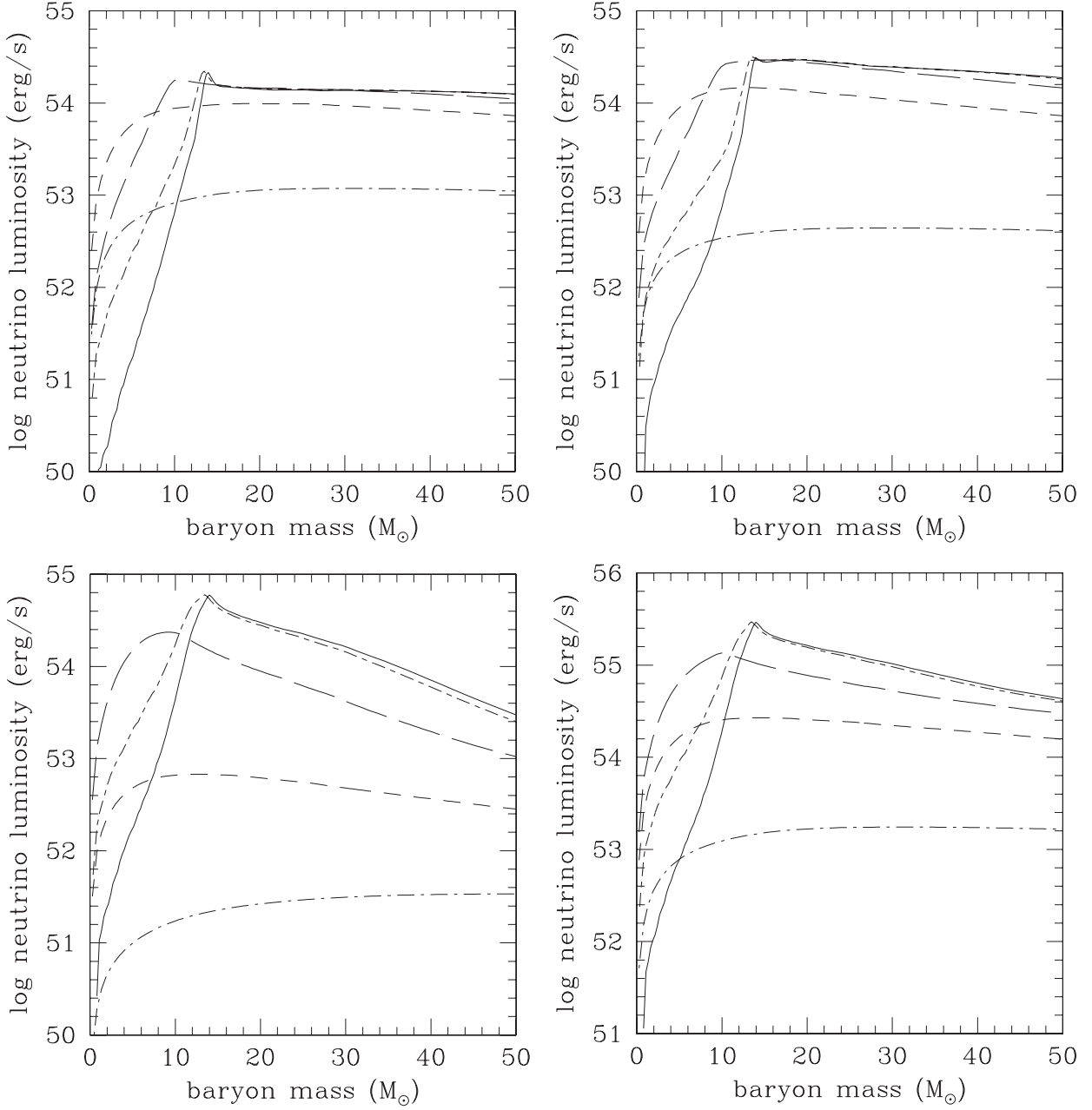


Fig. 7.— Profiles of neutrino luminosity for the model with $M_i = 375M_\odot$. Upper left, upper right, lower left and lower right panels are for ν_e , $\bar{\nu}_e$, ν_x and their sum, respectively, where ν_x stands for μ - and τ -neutrinos and anti-neutrinos. The notation of lines is the same as in Fig. 1.

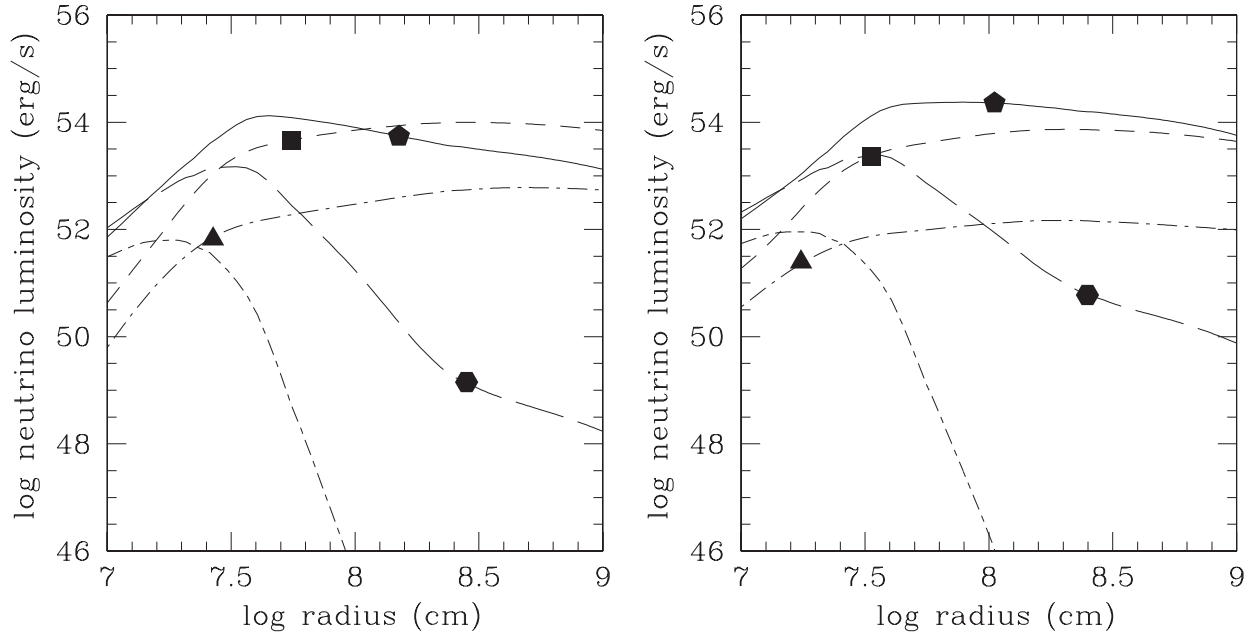


Fig. 8.— Profiles of the neutrino luminosity with different energies for the model with $M_i = 375M_\odot$ at $t = -12.3$ ms. Left and right panels are for ν_e and $\bar{\nu}_e$, respectively. In each panel, the dot-dashed line, short dashed line, solid line, long dashed line and short-long dashed line correspond to the neutrino luminosity with 2.51 MeV, 6.31 MeV, 15.8 MeV, 35.4 MeV and 70.7 MeV. The points on each line mark the locations of neutrino sphere for each energy.

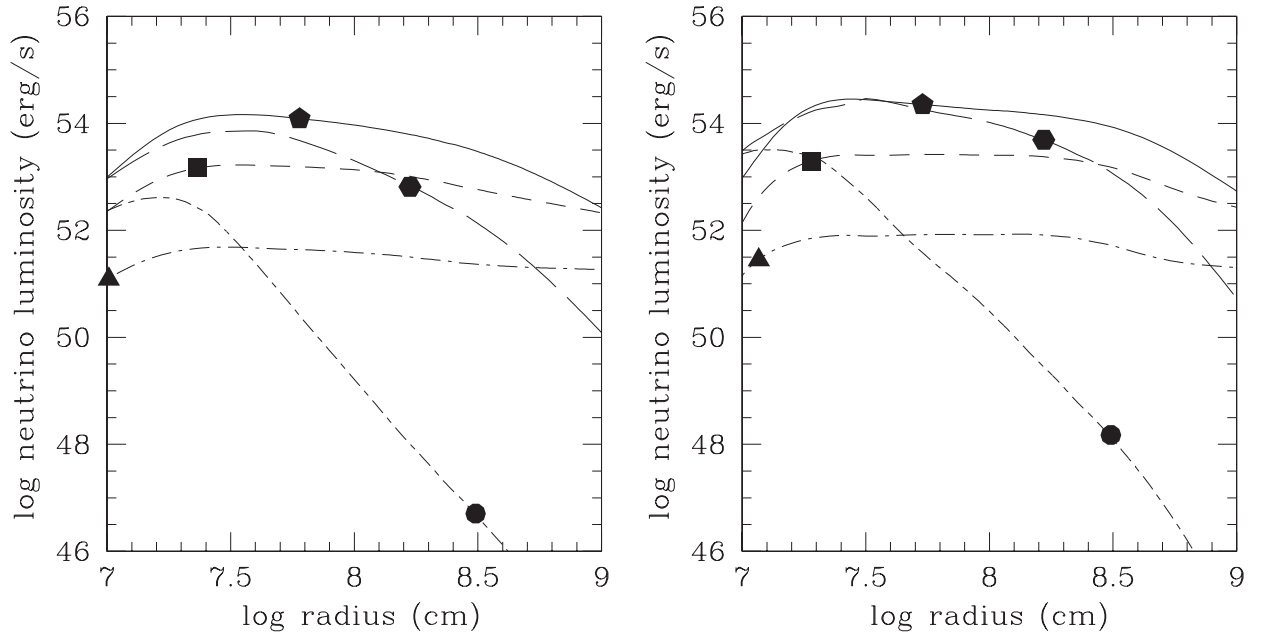


Fig. 9.— Profiles of the ν_x ($= \nu_\mu, \nu_\tau, \bar{\nu}_\mu, \bar{\nu}_\tau$) luminosity with different energies for the model with $M_i = 375M_\odot$ at $t = -12.3$ ms (left) and $t = -1.52$ ms (right). The notation of lines and points is the same as in Fig. 8.

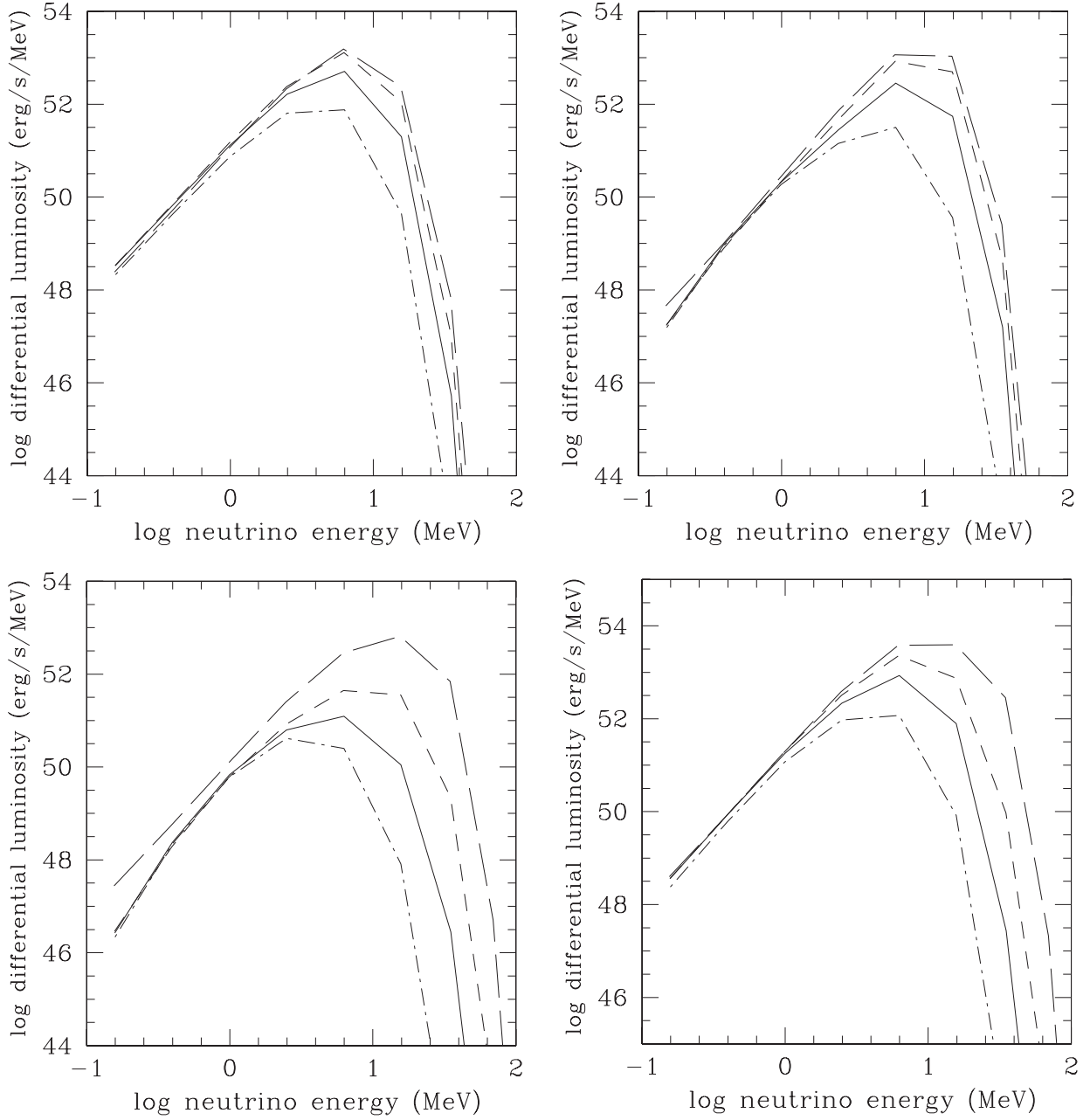


Fig. 10.— Spectra of emitted neutrinos. Upper left, upper right, lower left and lower right panels are for ν_e , $\bar{\nu}_e$, ν_x ($= \nu_\mu, \nu_\tau, \bar{\nu}_\mu, \bar{\nu}_\tau$) and their sum, respectively. The dot-dashed line, solid line, short dashed line and long dashed line represent, respectively, the spectra at $t = -239$ ms, $t = 0$ ms, $t = 60.3$ ms and $t = 85.0$ ms.

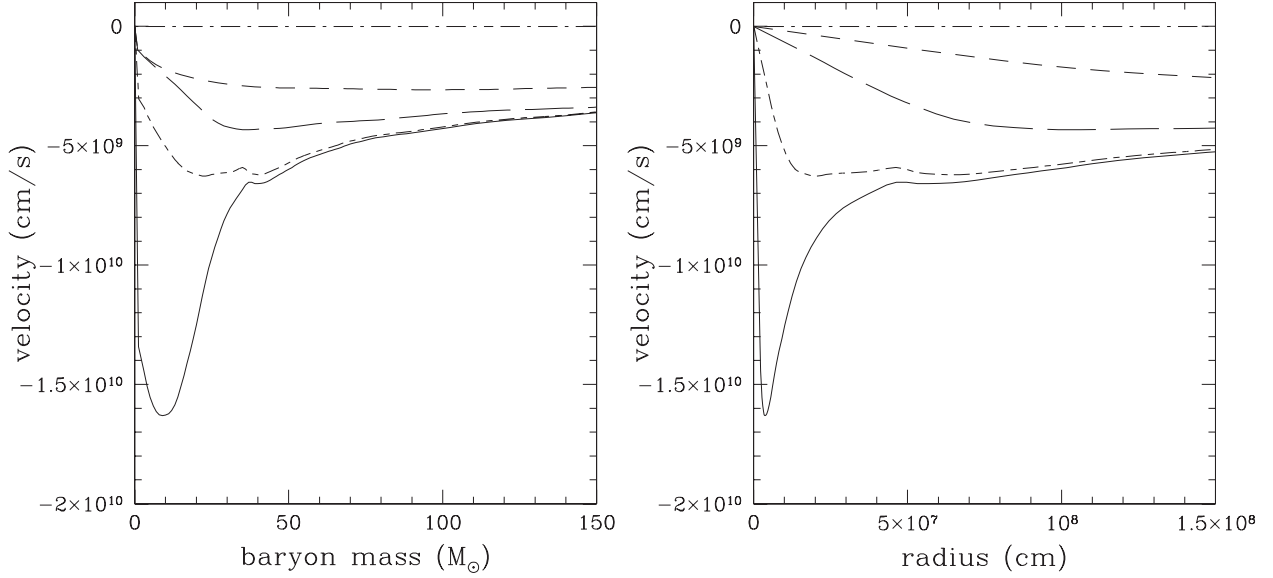


Fig. 11.— Profiles of the radial velocity for the model with $M_i = 10500M_\odot$. The line correspond, from top to bottom, to $t = -11.03$ s, $t = -59.8$ ms, $t = -14.0$ ms, $t = -1.27$ ms and $t = 0$ ms.

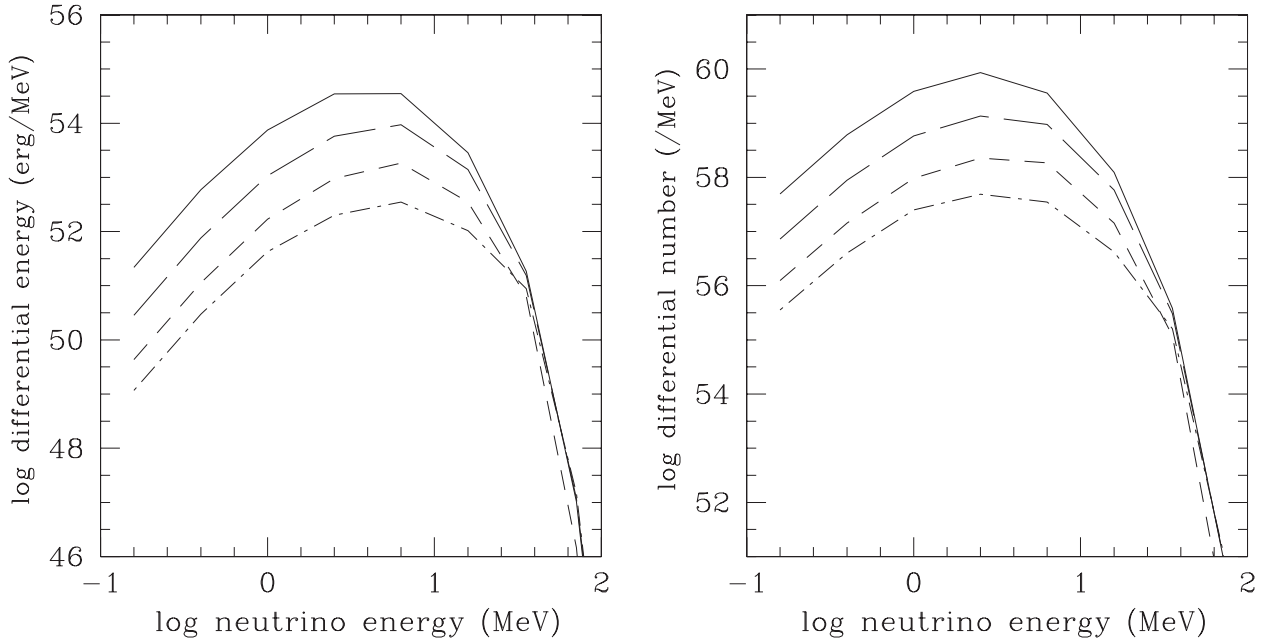


Fig. 12.— Neutrino energy (left) and number (right) spectra. The dot-dashed line, short dashed line, long dashed line and solid line represent, respectively, the models with $M_i = 375M_\odot$, $M_i = 1145M_\odot$, $M_i = 3500M_\odot$ and $M_i = 10500M_\odot$.

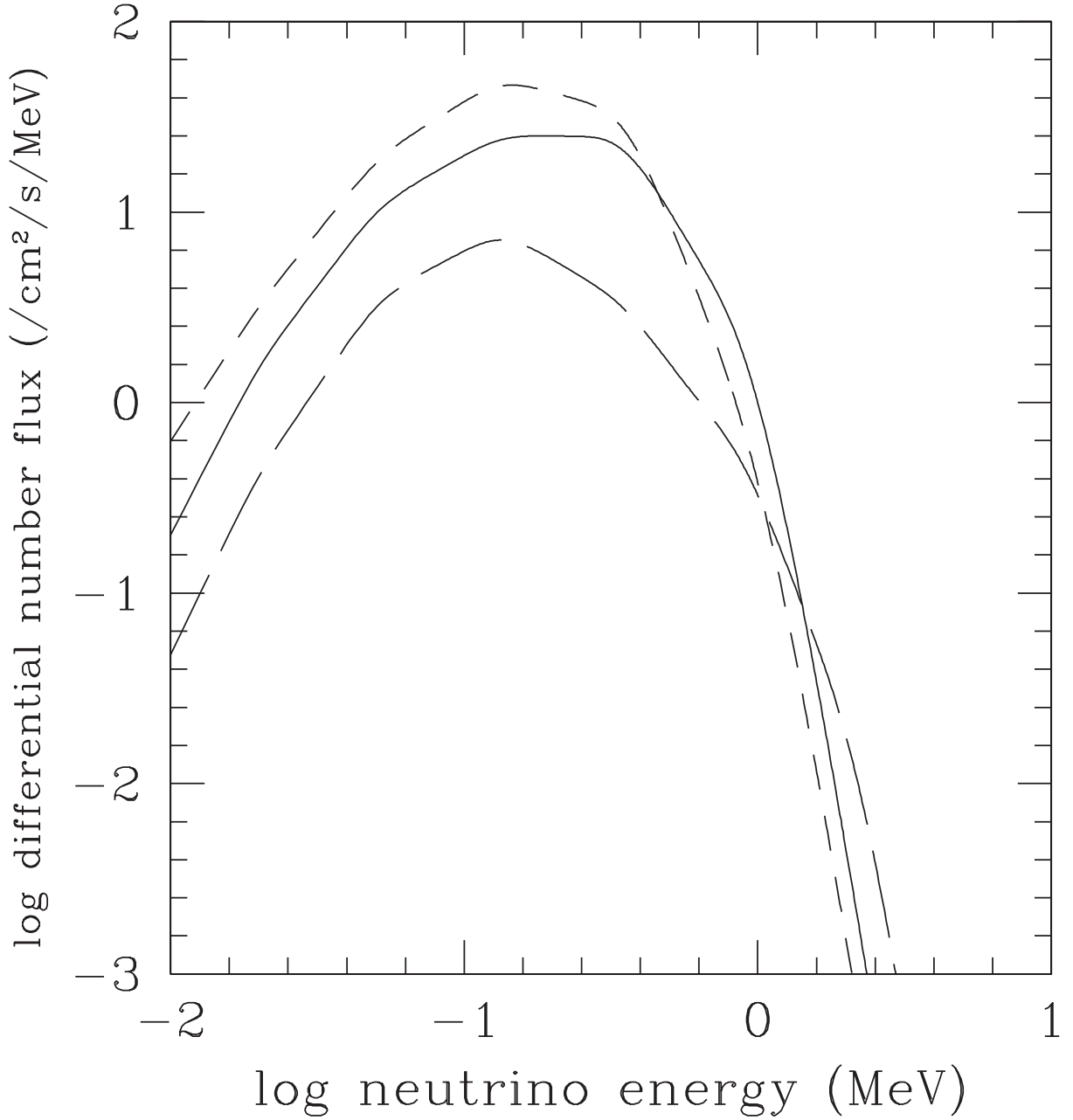


Fig. 13.— Relic neutrino number flux from Pop III massive stars (model A, $\beta = 1.35$). The short dashed line, solid line and long dashed line represent ν_e , $\bar{\nu}_e$ and ν_x , respectively.

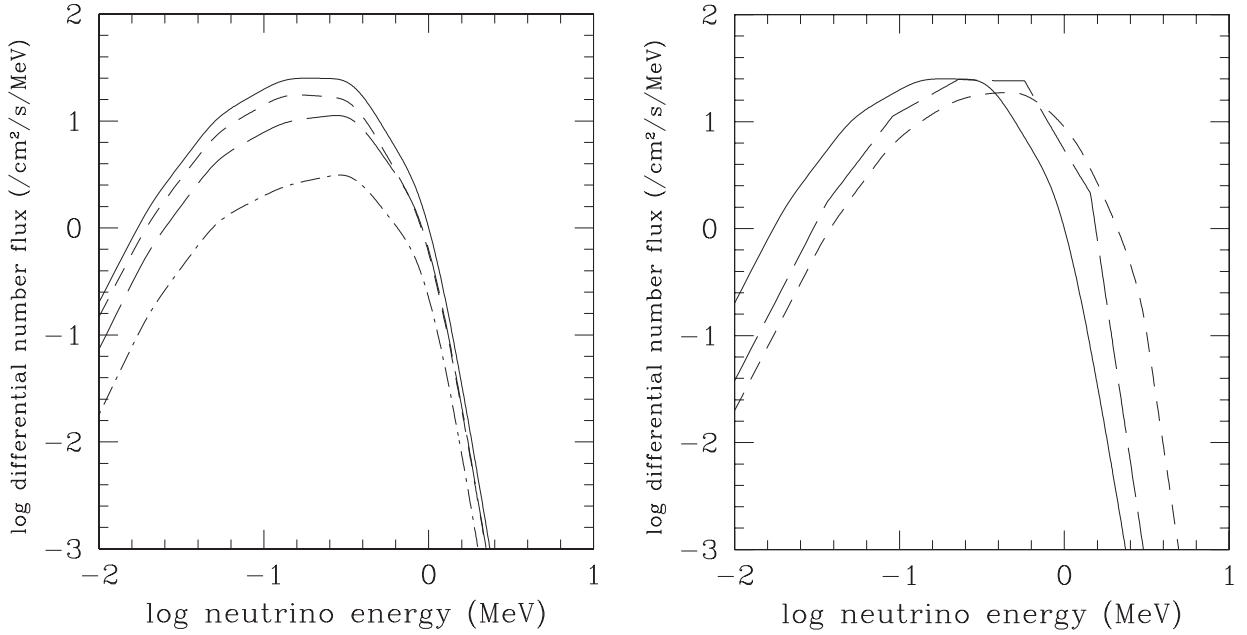


Fig. 14.— Relic $\bar{\nu}_e$ number fluxes from Pop III massive stars for various values of β and different star formation histories. The left panel shows the result of model A and the short dashed line, solid line, long dashed line and dot-dashed line correspond to $\beta = 1.1$, $\beta = 1.35$, $\beta = 2$ and $\beta = 3$, respectively. The right panel shows the result for $\beta = 1.35$ and the solid line, long dashed line, and short dashed line represent models A, B and C, respectively.